The Astrophysical Journal Letters, 949:L3 (8pp), 2023 May 20 https://doi.org/10.3847/2041-8213/acc4b6

Deep Synoptic Array Science: Discovery of the Host Galaxy of FRB 20220912A

Vikram Ravi[1,2], Morgan Catha[2], Ge Chen[1], Liam Connor[1], Jakob T. Faber[1], James W. Lamb[2], Gregg Hallinan[1,2], Charlie Harnach[2], Greg Hellbourg[1,2], Rick Hobbs[2], David Hodge[1], Mark Hodges[2], Casey Law[1,2], Paul Rasmussen[2], Kritti Sharma[1], Myles B. Sherman[1], Jun Shi[1], Dana Simard[1], Reynier Squillace[1], Sander Weinreb[1], David P. Woody[2], Nitika Yadlapalli[1]
(The Deep Synoptic Array team),
Tomas Ahumada[1], Dillon Dong[1], Christoffer Fremling[1], Yuping Huang[1], Viraj Karambelkar[1], and Jessie M. Miller[1]
[1] Cahill Center for Astronomy and Astrophysics, MC 249-17 California Institute of Technology, Pasadena, CA 91125, USA; vikram@caltech.edu
[2] Owens Valley Radio Observatory, California Institute of Technology, Big Pine, CA 93513, USA
Received 2022 November 16; revised 2023 March 2; accepted 2023 March 15; published 2023 May 17

Abstract

We report the detection and interferometric localization of the repeating fast radio burst (FRB) source FRB 20220912A during commissioning observations with the Deep Synoptic Array (DSA-110). Two bursts were detected from FRB 20220912A, one each on 2022 October 18 and 2022 October 25. The best-fit position is (R.A. J2000, decl. J2000) = (23:09:04.9, +48:42:25.4), with a 90% confidence error ellipse with radii $\pm 2''$ and $\pm 1''$ in R. A. and decl., respectively. The two bursts are polarized, and we find a Faraday rotation measure that is consistent with the low value of $+0.6$ rad m^{-2} reported by CHIME/FRB. The DSA-110 localization overlaps with the galaxy PSO J347.2702+48.7066 at a redshift $z = 0.0771$, which we identify as the likely host. PSO J347.2702+48.7066 has a stellar mass of approximately $10^{10} M_{\odot}$, modest internal dust extinction, and a star formation rate likely in excess of $0.1\,M_{\odot}$ yr^{-1}. The host-galaxy contribution to the dispersion measure is likely $\lesssim 50$ pc cm^{-3}. The FRB 20220912A source is therefore likely viewed along a tenuous plasma column through the host galaxy.

Unified Astronomy Thesaurus concepts: Compact objects (288); Radio interferometry (1346); Radio telescopes (1360); Radio transient sources (2008)

1. Introduction

Eight repeating sources of fast radio bursts (FRBs) have been localized to host galaxies (Chatterjee et al. 2017; Macquart et al. 2020; Marcote et al. 2020; Bhardwaj et al. 2021; Bhandari et al. 2022; Kirsten et al. 2022; Niu et al. 2022; Ravi et al. 2022). It is not yet established whether there are astrophysical differences between the progenitors of the few FRB sources that have been observed to repeat and the many FRB sources that have not yet been observed to repeat. Although it is likely that most FRB sources repeat at some level (Ravi 2019), repeating sources are different from apparent nonrepeaters in their burst morphologies and bandwidths (Pleunis et al. 2021) and in their repetition rates (James et al. 2020). No significant differences between the host galaxies of repeaters and apparent nonrepeaters are yet evident (Bhandari et al. 2022). The association of persistent radio sources with some repeaters may hint at a unique progenitor class (Law et al. 2022).

Repeating FRB sources offer the best means to identify the objects and mechanisms that can produce radio bursts with energy outputs in excess of $\sim 10^{35}$ erg on $\ll 1$ s timescales. This is particularly the case when observations of repeaters are placed in the rich context of milliarcsecond-scale localizations. For example, the association of FRB 20121102A with a star-forming region and compact persistent radio source within its dwarf host (Bassa et al. 2017), combined with its extreme and variable Faraday rotation measure (RM; Michilli et al. 2018), are suggestive of a young compact object within its birth supernova remnant (Chen et al. 2022 and references therein). The detection of microstructure in bursts from FRB 20200120E (Majid et al. 2021; Nimmo et al. 2022), together with its association with a globular cluster of M81 (Kirsten et al. 2022), suggest an origin in a recycled pulsar system. Despite its origin in an interarm region of its late-type host galaxy (Xu et al. 2022), FRB 20201124A illuminates extreme variability of its sub-astronomical-unit magnetoionic environment, suggestive of a magnetar/Be-star binary (Wang et al. 2022). Such observational diversity among the small sample of just eight localized sources motivates the characterization of a larger sample of host galaxies and environments of repeating FRBs.

FRB 20220912A is an intensely active repeating FRB source discovered by the CHIME/FRB collaboration (McKinven & Chime/Frb Collaboration 2022). Twelve bursts were detected in the 400–800 MHz band between 2022 September 12 and 2022 October 15. Throughout this Letter, unless otherwise indicated, we adopt the dispersion measure (DM) and RM derived by CHIME/FRB from the brightest reported burst, 219.46 pc cm^{-3} and $+0.6$ rad m^{-2}, respectively. On 2022 October 18, Herrmann (2022) reported the detection of 12 bursts within 49 hr of exposure at the Stockert telescope, with fluences >10 Jy ms in the 1330–1430 MHz band. A burst rate in excess of 400 hr^{-1} was found in the 1000–1500 MHz band in observations with the Five-hundred-meter Aperture Spherical Telescope (FAST; Zhang et al. 2022), and the Arecibo 12-m telescope was used to detect the source at 2.3 GHz (Perera et al. 2022). Deep limits on transient optical emission coincident with several radio bursts from FRB 20220912A were reported by Hiramatsu et al. (2023).

Here we report the detection and interferometric localization of FRB 20220912A during commissioning of the Deep

Table 1
Specifications of the DSA-110 during Commissioning Observations

Parameter	Value
Dish diameter (m)	4.65
Central frequency (MHz)	1405
Primary beam FWHM (deg)	3.4
Bandwidth (MHz)	187.5
Search SEFD (Jy)[a]	140
Search-beam channel width (kHz)	244.141
Search-beam time resolution (μs)	262.144
Search-beam width (arcsec)[b]	134
Number of search beams	256
Search-beam spacing (arcmin)	1
Maximum baseline (m)	2500
Synthesized beam[c]	$35\farcs4 \times 17\farcs6$ @ $83\fdg4$

Notes.
[a] System-equivalent flux density (SEFD) at boresight.
[b] This is in the east–west direction. The search beams are fan beams formed with an east–west array, and their sizes are only constrained by the primary beam in the north–south direction.
[c] Major- and minor-axis diameters at a decl. of $+48\fdg7$, assuming natural weighting. The position angle is measured east of north.

Synoptic Array (DSA-110). Preliminary results from this work were reported via Astronomer's Telegram (Ravi et al. 2022; Ravi 2022a, 2022b). In Section 2 we describe the DSA-110 (Section 2.1) and observations obtained of FRB 20220912A (Section 2.2) and present the detections (Section 2.3) and localizations (Section 2.4) of two bursts. In Section 3 we present observations of the likely host galaxy of FRB 20220912A, PSO J347.2702+48.7066, obtained at the W. M. Keck Observatory, together with modeling of fundamental properties of the host. We summarize and discuss implications of these results in Section 4. Throughout, we adopt a flat cosmology with parameters derived by Planck Collaboration et al. (2020), including a Hubble constant of $67.4\,\mathrm{km\,s^{-1}\,Mpc^{-1}}$ and a matter-density parameter of $\Omega_m = 0.315$.

2. DSA-110 Observations

2.1. Description of the DSA-110

The DSA-110[3] is a radio interferometer hosted at the Owens Valley Radio Observatory (OVRO). During the observations presented herein, the array was being commissioned with data from 48 core antennas and 15 outriggers being processed. A full description will be presented in V. Ravi et al. 2023, (in preparation), and we here include essential information to support the observational results for FRB 20220912A.

Essential specifications of the DSA-110 at the time of these observations are presented in Table 1. Each DSA-110 antenna is automatically steerable in elevation only and observes on the meridian. Each antenna is equipped with dual orthogonal linearly polarized receivers and ambient temperature amplifiers that deliver a typical system temperature of 25 K (Weinreb & Shi 2021). A real-time FRB search is enabled through the coherent combination of 48 core antennas located in an east–west line, with a maximum spacing of 400 m. Total-intensity data in 256 coherent, fan-shaped search beams are inspected in real time for FRBs, using a modified version of the `heimdall` software (Barsdell et al. 2012). Triggers from FRB candidates result in the storage of post-filterbank voltage data from the 48 core antennas and 15 outrigger antennas. The 4-bit voltage data are recorded for 61440 samples at 32.768 μs time resolution in 6144×30.518 kHz channels.

Data from all antennas (core and outriggers) are also continuously correlated in real time in the two linear polarizations only (no cross-polarization products), resulting in the production of visibility data fringe stopped on the meridian at the pointing center. Each FRB candidate is accompanied by the storage of 2 hr of visibility data surrounding the trigger time. These visibility data are used to solve for antenna-based complex gains at the trigger time using a sky model. Any >1 Jy calibrator source from the Very Large Array (VLA) calibrator manual that passes within the primary beam, represents >15% of the flux within the beam, and is classified as "P" or "S" for the VLA C configuration is also used to trigger the storage of 10 min of visibility data fringe stopped at the calibrator location. These visibility data are used to derive antenna-based band-pass calibrations for the beam former and for postprocessing of the voltage data.

2.2. Observations of FRB 20220912A

Following the report on FRB 20220912A by CHIME/FRB (McKinven & Chime/Frb Collaboration 2022) on 2022 October 15, we began a campaign of near-daily observations of transits of the source with the DSA-110. The array was pointed at a decl. of $48\fdg7$. We report on the period between 2022 October 15 and 2022 October 25, during which we observed seven transits of FRB 20220912A and detected two bursts with the real-time system. During each transit, the source was within the field of view of the search beams for 25.9 minutes. As these observations were undertaken during science commissioning and the precise search completeness was not quantified, we do not quote a derived burst rate from FRB 20220912A.

When not observing FRB 20220912A, the DSA-110 was primarily pointed at a decl. of $71\fdg6$. Daily band-pass calibration was made possible using observations of the source 3C309.1 (J1459+7140), which has a flux density of 7.6 Jy at a wavelength of 20 cm according to the VLA calibrator manual. Approximate polarization calibration was made possible using voltage data obtained on the standard sources 3C48 and 3C286 (Perley & Butler 2013) on 2022 October 20.

2.3. Two Burst Detections

We detected bursts from FRB 20220912A on 2022 October 18 (hereafter Burst 1) and on 2022 October 25 (hereafter Burst 2), on modified Julian dates (MJDs) 59,870.22278235404 and 59,877.203253573236, respectively. The arrival times correspond to 1530 MHz and the DSA-110 reference position of $-118\fdg283$ longitude, $+37\fdg2334$ latitude. Burst 1 was detected with a signal-to-noise ratio (S/N) of 12.2 and an approximate DM of 228 pc cm^{-3}, and Burst 2 was detected with an S/N of 8.5 and an approximate DM of 223 pc cm^{-3}. Despite the differences between these DMs and the structure-optimized DM reported by CHIME/FRB (McKinven & Chime/Frb Collaboration 2022), we associated these detections with FRB 20220912A based on the correspondance between the CHIME/FRB position and the detection search beam. We

[3] https://deepsynoptic.org

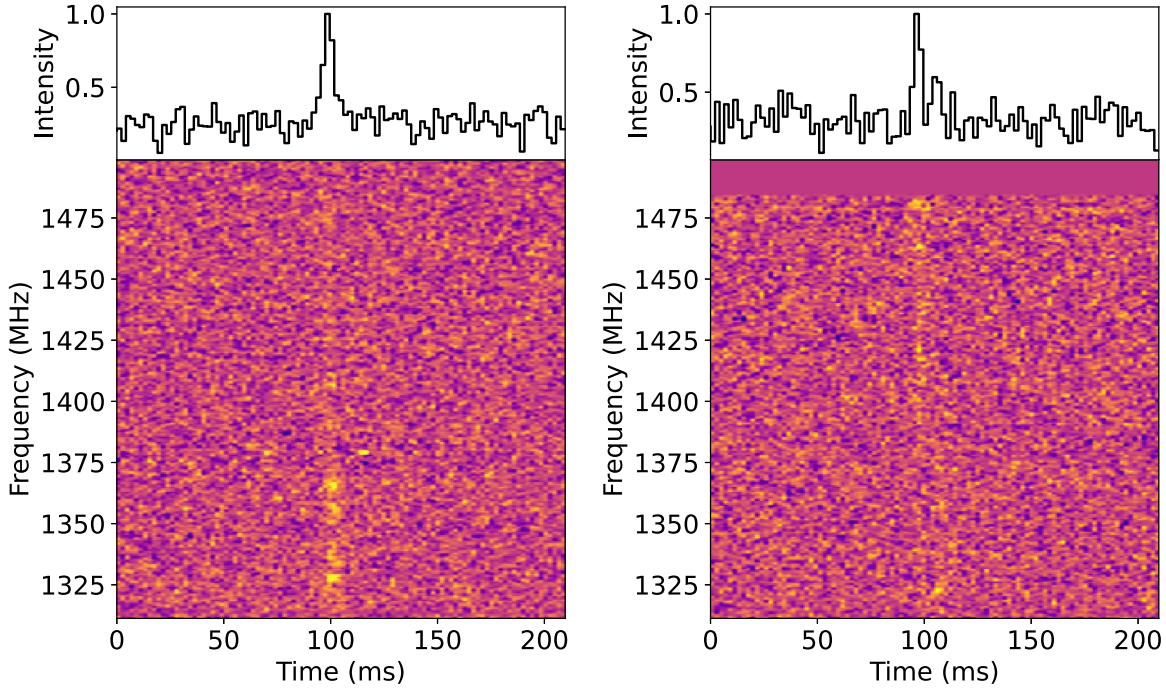

Figure 1. Dedispersed total-intensity dynamic spectra for Bursts 1 (left) and 2 (right) detected with the DSA-110 from FRB 20220912A. Both bursts have been dedispersed to DM = 219.46 pc cm^{-3}. Voltage data in one out of 16 sub-bands for Burst 2 were corrupted, resulting in the blanked data at the top of the band.

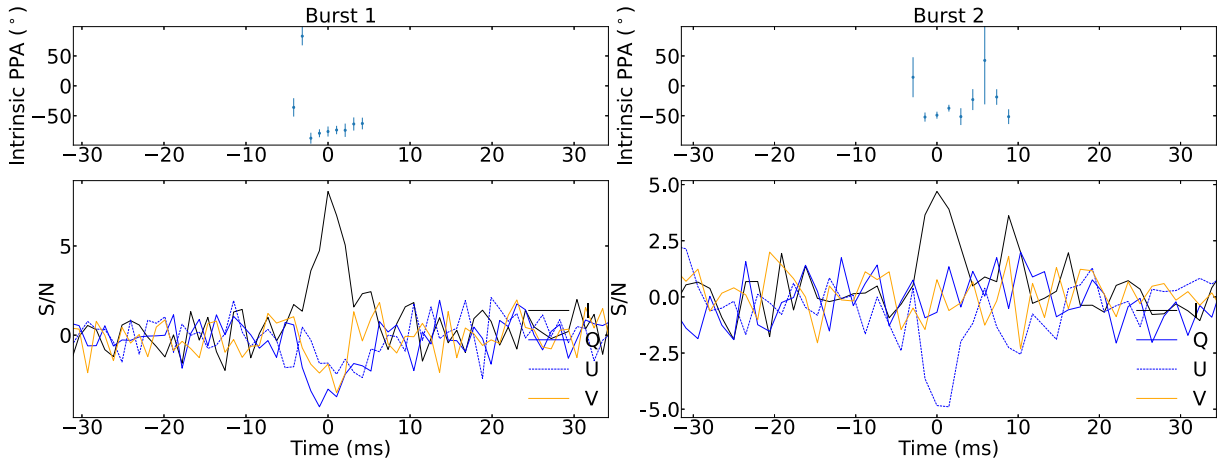

Figure 2. Polarization profiles of bursts 1 (left) and 2 (right) detected by the DSA-110 from FRB 20220912A. Both bursts have been dedispersed to DM = 219.46 pc cm^{-3}. The top panels show the absolute polarization position angle, and Stokes parameters are as labeled in the bottom panels. The polarized dynamic spectra of the bursts were corrected for the small RM reported by CHIME/FRB (0.6 rad m^{-2}).

attribute these differences to the time-frequency drifting common in repeating FRBs (e.g., Hessels et al. 2019).

Voltage data on each burst were coherently combined in the direction of the detection beams using the 48 core antennas only. Time-frequency data sets in all four Stokes parameters were formed with the native time and frequency resolutions. Incoherent dedispersion at the native time and frequency resolutions was applied. Flattening of the band passes in each received polarization was done on a per-antenna basis using observations of 3C309.1 on the same sidereal days as the burst detections. Voltage data obtained during transits of 3C48 and 3C286 were used for polarization calibration under the ideal feed assumption; coupling between the orthogonal polarizations is detected at only the percent level for DSA-110 (M. Sherman et al. 2023, in preparation). Full-Stokes spectra toward 3C48 and 3C286 were formed using the same beam-forming procedure as applied to the burst data. Spectra on 3C48 were used to verify the equalization of the amplitude gains in the two linear polarizations, and spectra on 3C286 were used to measure the frequency-dependent phase between the two polarizations.

Total-intensity dynamic spectra and temporal profiles are shown in Figure 1, and full-Stokes temporal profiles are shown in Figure 2. Voltage data in one out of 16 sub-bands for Burst 2 were corrupted, resulting in the reduced bandwidth evident in Figure 1. The two bursts exhibit marginally different morphologies and polarization characteristics. Burst 1 exhibits a single component, whereas Burst 2 potentially exhibits two components with visually different total-intensity spectra. For Burst 1, we measure a linear polarization fraction of 64% ± 18% and a circular polarization fraction of 41% ± 9%. For Burst 2, we measure a linear polarization fraction of

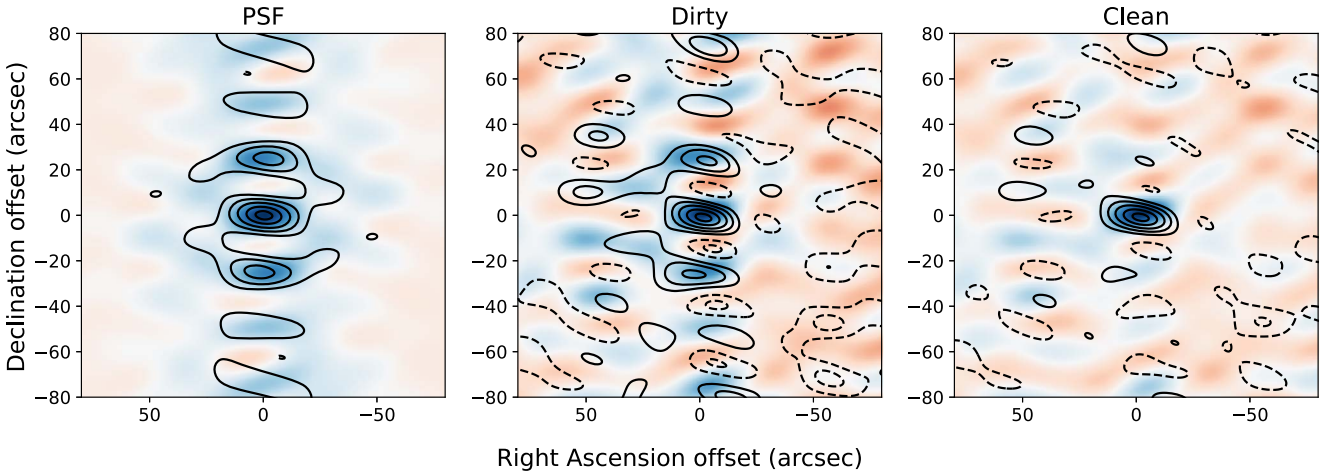

Figure 3. Dirty (middle) and clean (right) images of Burst 1 from FRB 20220912A, together with the DSA-110 PSF for Burst 1 (left). Contours are at −0.4, −0.2 (dashed), 0.2, 0.4, 0.6, 0.8, and 0.9 (solid) of the peak intensity. The burst images are centered on the coordinates (R.A. J2000, decl. J2000) = (23:09:04.9, +48:42:25.4).

73% ± 30%, with no significant circular polarization and a different polarization position angle. This is consistent with the report in Zhang et al. (2022) of substantially varying polarization properties between bursts from FRB 20220912A. Although these data have been corrected for an RM of +0.6 rad m^{-2} (McKinven & Chime/Frb Collaboration 2022), an independent RM search of each burst revealed measurements consistent with this value. These data do not have sufficiently high S/N for more detailed inferences to be made.

2.4. Interferometric Localization

We were able to derive arcsecond-scale localizations for the two bursts detected with DSA-110 from FRB 20220912A. The voltage data obtained for each burst from all core and outrigger antennas were dedispersed with DMs that maximized the S/N, and correlation products in each orthogonal linear polarization were formed and integrated over 8.36 ms centered on each burst arrival time. These correlation products were written into Common Astronomy Software Applications (CASA; THE CASA TEAM et al. 2022) measurement sets (MSs), and all further processing was done using `CASA` version 5.4.1. Band-pass calibrations were obtained using 10 minute observations of 3C309.1 on the same sidereal days as the burst detections and assuming a flat-spectrum point-source model. So-called "field" MSs were then generated using 10 minutes of visibility data surrounding the arrival times of each burst, fringe stopped at a 1 hr angle of 0 at the midpoint of the observation. Sky models based on the NRAO VLA Sky Survey (NVSS; Condon et al. 1998) were inserted into the field MSs, including all sources brighter than 30 mJy of any size. Extended sources were modeled as elliptical Gaussians. After band-pass calibration, the sky models were used to derive complex gain solutions for each antenna from the field MSs. The band-pass and gain calibration tables were then applied to the burst MSs. Wide-field images of the burst MSs 4.°5 in diameter with 4100 pixels per side were made using the `wsclean` software (Offringa et al. 2014) to crudely identify the locations of the bursts. The `CASA` task `tclean` was then used to make higher-resolution images 5′ and 1000 pixels per side centered on the approximate FRB positions. For these images, Briggs weighting with a robust parameter of 0.5 was used to optimize the point-spread function (PSF). All frequencies were weighted equally despite the apparent spectral structure of the bursts (Figure 1); although this results in lower-fidelity deconvolution, the effect is marginal given the small fractional bandwidth. Baselines shorter than 40 m were discarded due to spurious correlated power on short baselines. The localizations were derived by fitting two-dimensional Gaussians in the image plane to deconvolved burst images, derived from 10 image-plane CLEAN iterations.

The best-fit position for Burst 1 was (R.A. J2000, decl. J2000) = (23:09:04.90, +48:42:25.4), and the best-fit position for Burst 2 was (R.A. J2000, decl. J2000) = (23:09:04.88, +48:42:25.6).[4] Dirty and clean images of Burst 1, together with the PSF, are shown in Figure 3. In the wide-field `wsclean` images, the image S/N values for the bursts were 11 and 7, found after 10 image-plane CLEAN iterations and measured far from the sources. As the image of Burst 2 is of somewhat worse quality than that of Burst 1, we adopt the position of Burst 1 as the best-fit DSA-110 position of FRB 20220912A.

We verified the astrometric accuracy of our results in four ways. First, we compared images of the primary-beam full-width half-maximum (FWHM) areas made with the entire 2.1 s voltage data sets, and with the field MSs, and ensured that bright sources were detected at consistent positions. We then checked the efficacy of the gain calibrations derived from the field MSs by checking the positions of bright (>50 mJy) compact (<30″) NVSS sources within the primary-beam FWHM in images of these MSs against NVSS catalog positions. The results are shown in the top panel of Figure 4. Some offsets in derived positions due to the differing synthesized-beam shapes of the DSA-110 and NVSS are expected for resolved sources, and so this check is best used to search for systematic errors in the gain calibrations rather than quantify the localization accuracy. Instead, we checked the absolute astrometry by forming MSs on and imaging two compact bright sources from the Radio Fundamental Catalog

[4] Ravi (2022b) issued a correction to the preliminary position for Burst 1 quoted in Ravi (2022a). The tests on PSR J1935+1616 described here revealed an error in the calculation of absolute time in the voltage imaging pipeline (Ravi 2022b). This error resulted in a systematic error in the source positions that was not present in the positions measured by the field-imaging pipeline. The tests reported here confirm that both pipelines produce consistent astrometry.

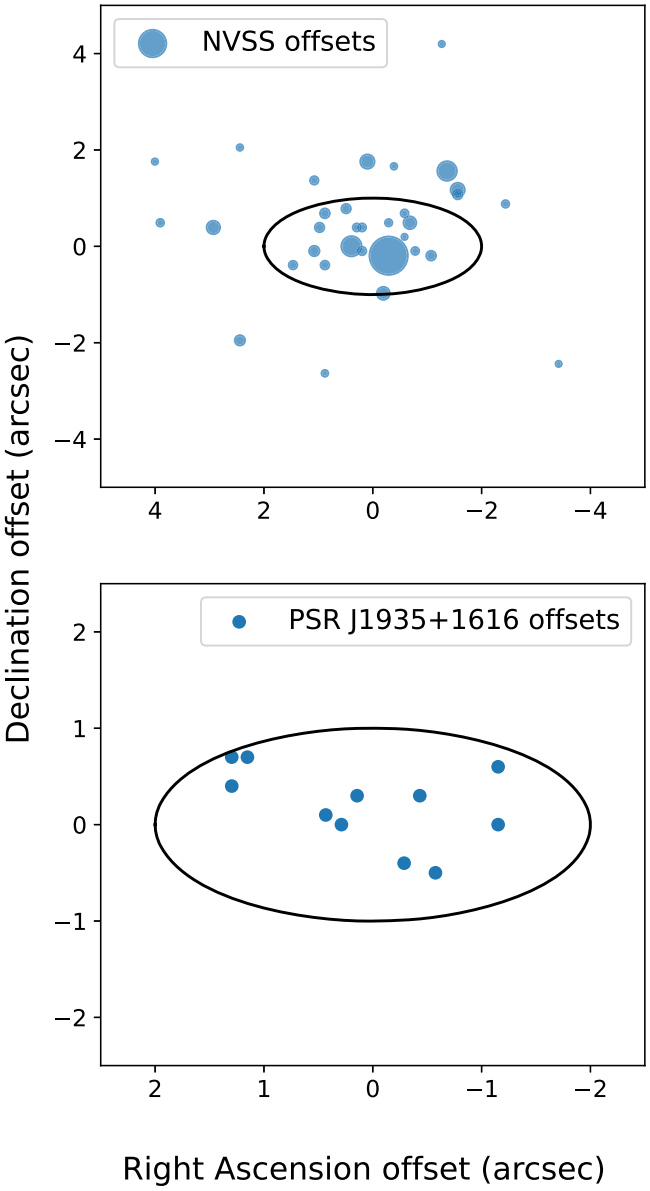

Figure 4. Two different verifications of the accuracy with which DSA-110 recovers the positions of known astronomical sources. Both panels show offsets of sources in DSA-110 data from their true positions and the approximate 90% confidence error ellipse quoted for the localization of FRB 20220912A. Top: offsets of sources from cataloged positions in the NRAO VLA Sky Survey (NVSS; Condon et al. 1998) in a 10 min DSA-110 image formed from data taken around Burst 1. Only sources with cataloged flux densities >50 mJy and measured major-axis diameters <30, within 2° of the pointing center, were considered. The symbol size is proportional to flux density. Bottom: offsets of 11 pulses from PSR J1935+1616 localized between 2022 October 22 and 2022 October 25 from the true pulsar position, corrected for proper motion. All pulses were localized using exactly the same pipeline as for the bursts from FRB 20220912A.

(rfc_2022c), J2258+4937 and J2325+4806. These sources are close in decl. to FRB 20220912A and thus transit through similar portions of the DSA-110 primary beam, and are close in R.A. and thus could be calibrated using gains from the field MSs. The derived position offsets were 0.″7 and 0.″4 respectively from the rfc_2022c positions on 2022 October 18, and 0.″5 and 0.″6 respectively on 2022 October 25. We also conducted observations of the bright pulsar J1935+1616 over three transits between 2022 October 22 and 2022 October 25, and performed a localization analysis on 11 automatically

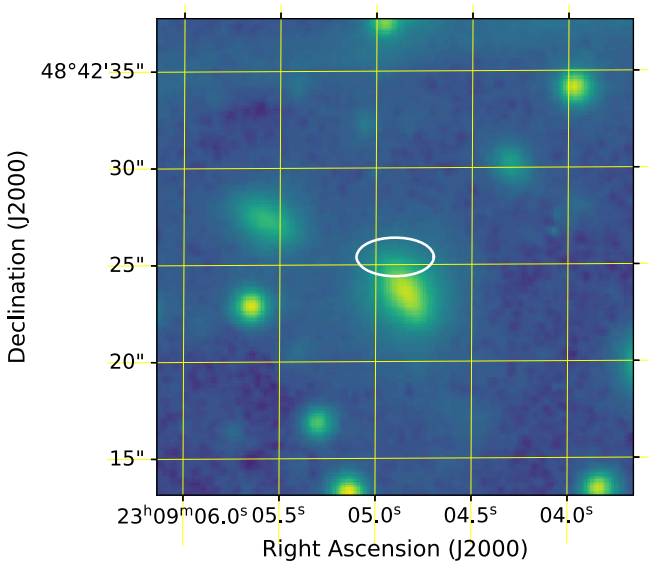

Figure 5. Deep optical *R*-band image obtained with Keck II/ESI (limiting magnitude $R \sim 26$) of the localization region of FRB 20220912A. The approximate 90% error ellipse for the DSA-110 localization of FRB 20220912A is shown in white, to the north of the galaxy PSO J347.2702+48.7066.

detected single pulses in exactly the same way as for the FRB 20220912A burst detections. The resulting offsets from the true position of PSR J1935+1616 (Manchester et al. 2005), corrected for proper motion, are shown in the bottom panel of Figure 4. The S/Ns of these pulses ranged between 10 and 21.

Given these tests, we find no evidence for systematic offsets or effects of non-Gaussian noise. We therefore quote the localization as measured along with a conservative theoretical estimate of the statistical uncertainty for a source with an image S/N of 10. Conservatively, the standard error in each coordinate is given by half the synthesized-beam FWHM (Reid et al. 1988). Each error is scaled by 2.14 (e.g., Condon et al. 1998) to derive diameters of the 90% confidence error ellipse. We quote an approximate 90% confidence error ellipse with diameters of 4″ in R.A. and 2″ in decl., as shown in Figure 4.

3. The Host Galaxy of FRB 20220912A

The DSA-110 position for FRB 20220912A overlaps just a single galaxy, PSO J347.2702+48.7066 (Figure 5). This galaxy, with an *r*-band magnitude of 19.65 (Magnier et al. 2020), was also noted as a promising host by McKinven & Chime/Frb Collaboration (2022). We therefore consider PSO J347.2702+48.7066, hereafter PSO J347+48, as the likely host galaxy of FRB 20220912A. For example, an analysis of galaxy detections in Pan-STARRS data near the DSA-110 position for FRB 20220912A with the probabilistic association of transients to their hosts (PATH; Aggarwal et al. 2021) with standard priors, the localization region described above, and a 50% chance of the host being unseen indicates a 5% false-association probability. In this section we present and interpret optical observations of PSO J347+48. Fundamental parameters that we derive for this galaxy are given in Table 2.

3.1. Optical Observations

We obtained an optical image of PSO J347+48 in the "Ellis-*R*" filter of the Echellette Spectrograph and Imager on the Keck

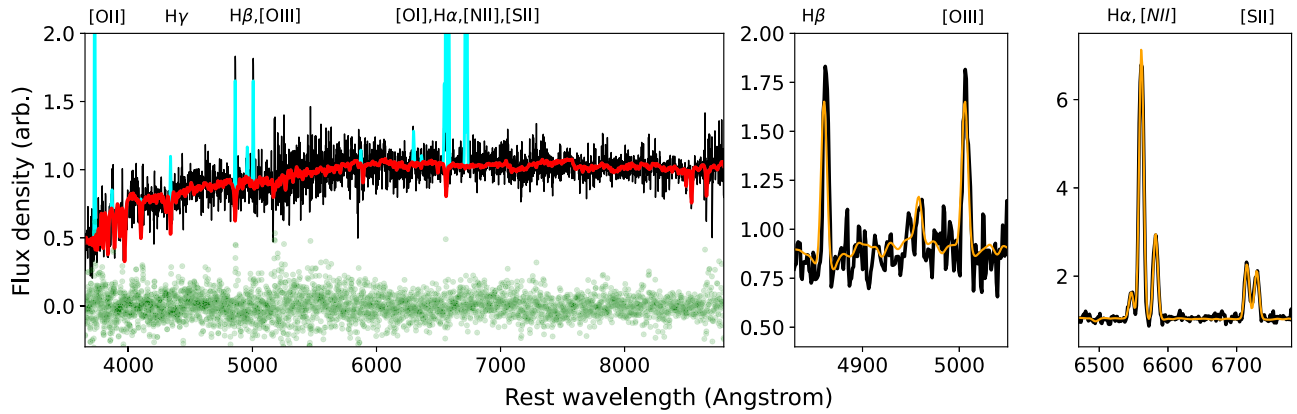

Figure 6. Optical spectrum of the central ∼1 arcsec^2 of the host galaxy of FRB 20220912A, PSO J347.2702+48.7066, obtained with Keck I/LRIS. The left panel shows the spectrum in black, the `pPXF` fit to the stellar continuum in red, and the `pPXF` fit to the nebular emission lines in cyan. The fit residuals are shown as green points. Selected emission lines are indicated. The middle and right panels show zoomed-in views of certain emission lines (black), with the total `pPXF` fit in orange.

Table 2
Observed and Derived Parameters of PSO J347.2702+48.7066

Parameter	Value
Redshift	0.0771(1)
Luminosity distance (Mpc)	362.4(1)
Effective radius (kpc)	2.2(1)
$\log M_*$	10.0(1)
Internal A_V	0.5
$\log Z$	$-0.8^{-0.3}_{-0.6}$
SFR ($M_\odot$ yr^{-1})	$\gtrsim$0.1
BPT classification	Composite

Note. Uncertainties in the last significant figures are given in parentheses.

II Telescope (Keck II/ESI; Sheinis et al. 2002). Four 300 s exposures were obtained on 2022 October 24 at an air mass of 1.45 in conditions of 0.″8 seeing. The data were bias subtracted, flat fielded, combined, and registered using a custom `astropy`-based pipeline (Astropy Collaboration et al. 2022). An astrometric solution was obtained using the ten nearest unsaturated Gaia Data Release 3 (Gaia Collaboration et al. 2022) stars to the center of PSO J347+48. The image is shown in Figure 5, and an approximate calibration against Gaia data implies a limiting magnitude of 26. There is no evidence for any object besides PSO J347+48 within the DSA-110 localization region of FRB 20220912A.

We obtained an optical spectrum of PSO J347+48 using the Low Resolution Imaging Spectrometer on the Keck I Telescope (Keck I/LRIS; Oke et al. 1995). A single 300 s exposure was obtained on 2022 October 19 in conditions of 0.″9 seeing at an air mass of 1.15, using a 1″ slit at a position angle of 254.°7. Light was split between the blue and red arms using the D560 dichroic and dispersed using the 400/3400 grism on the blue arm and the 400/8500 grating on the red arm. The line FWHM was approximately 7 Å. The data were processed using standard techniques with the `lpipe` software (Perley 2019); flux calibration was carried out using observations of the standard star BD+28 4211. A spectrum was extracted from the central square arcsecond of the galaxy; this is shown in Figure 6.

Several emission lines are evident in the spectrum of PSO J347+48, at a redshift of 0.0771 ± 0.0001. We measure

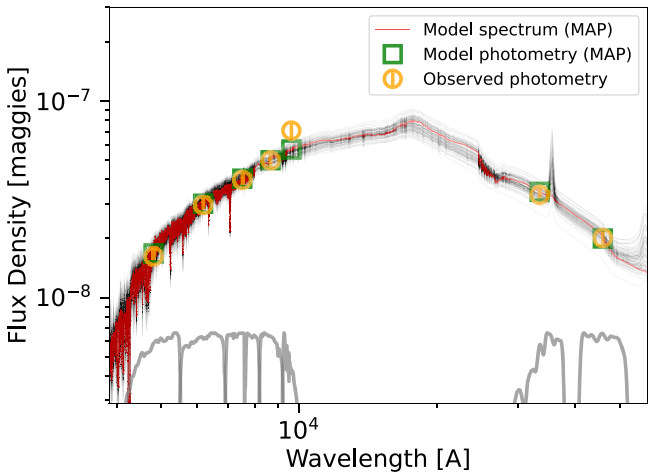

Figure 7. Results of a `Prospector` fit to the optical/IR spectral energy distribution (SED) of the host galaxy of FRB 20220912A, PSO J347.2702+48.7066. The SED measurements from archival PanSTARRS and WISE data are shown in orange, together with representative 10% errors. Filter transmission curves are shown in gray. The maximum a posteriori probability (MAP) model photometry is shown in green, together with the MAP spectrum in red. One hundred spectra generated from draws from the posterior distributions on the model parameters are shown in black.

an Hα line flux of $(1.23 \pm 0.05) \times 10^{-15}$ erg s^{-1} cm^{-2}. The line ratios $\log([\mathrm{O\,III}]/\mathrm{H}\beta) = 0.00 \pm 0.05$, $\log([\mathrm{N\,II}]/\mathrm{H}\alpha) = -0.04 \pm 0.01$, $\log([\mathrm{S\,II}]/\mathrm{H}\alpha) = -0.43 \pm 0.02$, and $\log([\mathrm{O\,I}]/\mathrm{H}\alpha) = -1.2 \pm 0.1$ imply a composite Baldwin–Phillips–Terlevich (BPT) classification (Kauffmann et al. 2003; Kewley et al. 2006). A two-dimensional Sérsic profile fit to the morphology of PSO J347+48 in the Keck II/ESI image, combined with the redshift measurement, indicates an effective radius of 2.2 ± 0.1 kpc. This is consistent with the $z \sim 0$ size −mass relation for late-type galaxies (Shen et al. 2003). The Hα line flux implies a star formation rate in the central square arcsecond of the galaxy of approximately 0.1 $M_\odot$ yr^{-1}, assuming no active galactic nucleus contribution and using a conversion factor consistent with Heintz et al. (2020). We note that the Keck I/LRIS two-dimensional spectrum shows evidence for off-nuclear Hα emission. Assuming a disklike galaxy, the inclination derived from a half-light isophote fit is 51°.

3.2. Host-galaxy Modeling

We performed a fit to the optical spectrum of PSO J347+48 using the latest iteration of the penalized pixel fitting code `pPXF` (Cappellari 2022) to jointly fit the stellar continuum and nebular emission. We adopted the default MILES stellar templates and ran the fit using recommended procedures and parameters. The fit results are shown in Figure 6. An internal dust extinction corresponding to $A_V = 0.5$ was found, and the fit results were also used for the redshift, line-flux, and line-ratio measurements given above.

We then fit archival photometry of PSO J347+48 from the Pan-STARRS (Magnier et al. 2020) and ALLWISE (Cutri et al. 2021) source catalogs using the `Prospector` stellar population synthesis modeling code (Johnson et al. 2021). Although the galaxy is marginally detected in 2MASS images, it is not cataloged, and we thus did not consider photometry from 2MASS data. ALLWISE detections in bands $w1$ and $w2$ were used, together with all five Pan-STARRS bands. We ran Prospector using recommended techniques and standard priors with a "delay-tau" parametric star formation history and sampled from the posterior using emcee (Foreman-Mackey et al. 2013). We fixed the internal dust attenuation to the `pPXF` result and included a model for dust reradiation in the likelihood. Results for the galaxy stellar mass and metallicity are given in Table 2. The star formation history was poorly constrained by the fit. The spectral energy distribution of PSO J347+48 is shown in Figure 7, together with the results from the Prospector analysis.

4. Summary and Discussion

Two bursts detected by the DSA-110 from the repeating source FRB 20220912A have been used to localize it to (R.A. J2000, decl. J2000) = (23:09:04.90, +48:42:25.4). The 90% confidence error ellipse has radii $\pm 2''$ and $\pm 1''$ in R.A. and decl., respectively. The localization is consistent with a single host galaxy, PSO J347.2702+48.7066, at $z = 0.0771 \pm 0.0001$. The galaxy has a stellar mass of $\log M_* = 10.0 \pm 0.1$ and an effective radius of 2.2 ± 0.1 kpc. Nebular emission lines from the nucleus of this galaxy indicates a "composite" BPT classification.

The redshift we find for the FRB host galaxy implies that the DM contributed by the host along the burst sight line is low. The extragalactic DM, $\mathrm{DM_{cosmic}}$, of FRB 20220912A is approximately 85 pc cm^{-3} (Cordes & Lazio 2002; Yao et al. 2017), assuming a modest contribution from the Milky Way halo of 10 pc cm^{-3} (Keating & Pen 2020). This extragalactic DM is likely dominated by diffuse intergalactic gas. For example, if we set the fraction of cosmic baryons in intergalactic gas to 70% following Macquart et al. (2020; i.e., $f_d = 0.7$ in their Equation (2)), the predicted $\mathrm{DM_{cosmic}}$ for $z = 0.0771$ is 55 pc cm^{-3}, implying a host DM contribution of 30 pc cm^{-3}. More conservatively, the 90% confidence lower limit on $\mathrm{DM_{cosmic}}$ using the model[5] for $\mathrm{DM_{cosmic}}(z)$ presented in Macquart et al. (2020) is 32 pc cm^{-3}, implying a 90% confidence upper limit on the host DM of 53 pc cm^{-3}.

The host galaxy and environment of FRB 20220912A appears unremarkable in the context of FRB hosts, repeating or so far nonrepeating (Bhandari et al. 2022). The low host DM of FRB 20220912A implies a tenuous plasma column toward the source within the host. The small magnitude of the RM reported by McKinven & Chime/Frb Collaboration (2022) and confirmed by us, consistent with a negligible extragalactic RM of $\lesssim O(10)$ rad m^{-2}, is consistent with the low host DM. The small RM also suggests that the variable polarization properties evident between the bursts detected from FRB 20220912A (Zhang et al. 2022) are an intrinsic effect in the source rather than due to propagation. Our results further suggest that repeating sources like FRBs 20121102A and 20190520B, with large local DMs and RMs and host galaxies with high specific star formation rates, are not common. Instead, the host DM of FRB 20220912A is consistent with expectations for typical late-type galaxies, like the host we report, if the progenitor class traces stellar mass (Xu & Han 2015; Walker et al. 2020; Mo et al. 2023). As the sample of accurately localized repeating FRBs expands, more detailed comparisons with the host-galaxy and host-environment properties of so far nonrepeating FRBs and other transient populations can be made (e.g., Bhandari et al. 2022). This will provide fresh insight into the origins of active FRB repetition.

The authors thank staff members of the Owens Valley Radio Observatory and the Caltech radio group, including Kristen Bernasconi, Stephanie Cha-Ramos, Sarah Harnach, Tom Klinefelter, Lori McGraw, Corey Posner, Andres Rizo, Michael Virgin, Scott White, and Thomas Zentmyer. Their tireless efforts were instrumental to the success of the DSA-110. The DSA-110 is supported by the National Science Foundation Mid-Scale Innovations Program in Astronomical Sciences (MSIP) under grant AST-1836018. We acknowledge use of the VLA calibrator manual and the radio fundamental catalog. Some of the data presented herein were obtained at the W. M. Keck Observatory, which is operated as a scientific partnership among the California Institute of Technology, the University of California and the National Aeronautics and Space Administration. The Observatory was made possible by the generous financial support of the W. M. Keck Foundation.

Facilities: Keck:I (LRIS), Keck:II (ESI).

Software: astropy (Astropy Collaboration et al. 2022), CASA (THE CASA TEAM et al. 2022), frb, heimdall (Barsdell et al. 2012), lpipe (Perley 2019), pPXF (Cappellari 2022), Prospector (Johnson et al. 2021), wsclean (Offringa et al. 2014).

ORCID iDs

Vikram Ravi https://orcid.org/0000-0002-7252-5485
Ge Chen https://orcid.org/0000-0003-2867-4544
Liam Connor https://orcid.org/0000-0002-7587-6352
James W. Lamb https://orcid.org/0000-0002-5959-1285
Gregg Hallinan https://orcid.org/0000-0002-7083-4049
Casey Law https://orcid.org/0000-0002-4119-9963
Kritti Sharma https://orcid.org/0000-0002-4477-3625
Myles B. Sherman https://orcid.org/0000-0002-6573-7316
Jun Shi https://orcid.org/0000-0003-1647-7762
Dana Simard https://orcid.org/0000-0002-8873-8784
Reynier Squillace https://orcid.org/0000-0001-6748-5290
Nitika Yadlapalli https://orcid.org/0000-0003-3255-4617
Dillon Dong https://orcid.org/0000-0001-9584-2531
Christoffer Fremling https://orcid.org/0000-0002-4223-103X
Yuping Huang https://orcid.org/0000-0003-4267-6108
Viraj Karambelkar https://orcid.org/0000-0003-2758-159X
Jessie M. Miller https://orcid.org/0000-0001-8840-922X

[5] The model is implemented in https://github.com/FRBs/FRB.

References

Aggarwal, K., Budavári, T., Deller, A. T., et al. 2021, ApJ, 911, 95
Astropy Collaboration, Price-Whelan, A. M., Lim, P. L., et al. 2022, ApJ, 935, 167
Barsdell, B. R., Bailes, M., Barnes, D. G., et al. 2012, MNRAS, 422, 379
Bassa, C. G., Tendulkar, S. P., Adams, E. A. K., et al. 2017, ApJL, 843, L8
Bhandari, S., Heintz, K. E., Aggarwal, K., et al. 2022, AJ, 163, 69
Bhardwaj, M., Kirichenko, A. Y., Michilli, D., et al. 2021, ApJL, 919, L24
Cappellari, M. 2022, arXiv:2208.14974
Chatterjee, S., Law, C. J., Wharton, R. S., et al. 2017, Natur, 541, 58
Chen, G., Ravi, V., & Hallinan, G. W. 2022, arXiv:2201.00999
Condon, J. J., Cotton, W. D., Greisen, E. W., et al. 1998, AJ, 115, 1693
Cordes, J. M., & Lazio, T. J. W. 2002, arXiv:astro-ph/0207156
Cutri, R. M., Wright, E. L., Conrow, T., et al. 2021, yCat, II/328
Foreman-Mackey, D., Hogg, D. W., Lang, D., et al. 2013, PASP, 125, 306
Gaia Collaboration, Vallenari, A., Brown, A. G. A., et al. 2022, arXiv:2208.00211
Heintz, K. E., Prochaska, J. X., Simha, S., et al. 2020, ApJ, 903, 152
Herrmann, W. 2022, ATel, 15691
Hessels, J. W. T., Spitler, L. G., Seymour, A. D., et al. 2019, ApJL, 876, L23
Hiramatsu, D., Berger, E., Metzger, B. D., et al. 2023, ApJL, 957, L28
James, C. W., Osłowski, S., Flynn, C., et al. 2020, MNRAS, 495, 2416
Johnson, B. D., Leja, J., Conroy, C., et al. 2021, ApJS, 254, 22
Kauffmann, G., Heckman, T. M., Tremonti, C., et al. 2003, MNRAS, 346, 1055
Keating, L. C., & Pen, U.-L. 2020, MNRAS, 496, L106
Kewley, L. J., Groves, B., Kauffmann, G., et al. 2006, MNRAS, 372, 961
Kirsten, F., Marcote, B., Nimmo, K., et al. 2022, Natur, 602, 585
Law, C. J., Connor, L., & Aggarwal, K. 2022, ApJ, 927, 55
Macquart, J.-P., Prochaska, J. X., McQuinn, M., et al. 2020, Natur, 581, 391
Magnier, E. A., Schlafly, E. F., Finkbeiner, D. P., et al. 2020, ApJS, 251, 6
Majid, W. A., Pearlman, A. B., Prince, T. A., et al. 2021, ApJL, 919, L6
Manchester, R. N., Hobbs, G. B., Teoh, A., et al. 2005, AJ, 129, 1993
Marcote, B., Nimmo, K., Hessels, J. W. T., et al. 2020, Natur, 577, 190
McKinven, R. & Chime/Frb Collaboration 2022, ATel, 15679
Michilli, D., Seymour, A., Hessels, J. W. T., et al. 2018, Natur, 553, 182
Mo, J.-F., Zhu, W., Wang, Y., et al. 2023, MNRAS, 518, 539
Nimmo, K., Hessels, J. W. T., Kirsten, F., et al. 2022, NatAs, 6, 393
Niu, C.-H., Aggarwal, K., Li, D., et al. 2022, Natur, 606, 873
Offringa, A. R., McKinley, B., Hurley-Walker, N., et al. 2014, MNRAS, 444, 606
Oke, J. B., Cohen, J. G., Carr, M., et al. 1995, PASP, 107, 375
Perera, B., Perillat, P., Fernandez, F., et al. 2022, ATel, 15734
Perley, D. A. 2019, PASP, 131, 084503
Perley, R. A., & Butler, B. J. 2013, ApJS, 206, 16
Pleunis, Z., Good, D. C., Kaspi, V. M., et al. 2021, ApJ, 923, 1
Planck Collaboration, Aghanim, N., Akrami, Y., et al. 2020, A&A, 641, A6
Ravi, V. 2019, NatAs, 3, 928
Ravi, V. 2022a, ATel, 15693
Ravi, V. 2022b, ATel, 15716, 1
Ravi, V., Karambelkar, V., Mena, T. A., et al. 2022, ATel, 15720
Ravi, V., Law, C. J., Li, D., et al. 2022, MNRAS, 513, 982
Reid, M. J., Schneps, M. H., Moran, J. M., et al. 1988, ApJ, 330, 809
Sheinis, A. I., Bolte, M., Epps, H. W., et al. 2002, PASP, 114, 851
Shen, S., Mo, H. J., White, S. D. M., et al. 2003, MNRAS, 343, 978
THE CASA TEAM, Bean, B., Bhatnagar, S., et al. 2022, PASP, 134, 114501
Walker, C. R. H., Ma, Y.-Z., & Breton, R. P. 2020, A&A, 638, A37
Wang, F. Y., Zhang, G. Q., Dai, Z. G., et al. 2022, NatCo, 13, 4382
Weinreb, S., & Shi, J. 2021, ITMTT, 69, 2345
Xu, H., Niu, J. R., Chen, P., et al. 2022, Natur, 609, 685
Xu, J., & Han, J. L. 2015, RAA, 15, 1629
Yao, J. M., Manchester, R. N., & Wang, N. 2017, ApJ, 835, 29
Zhang, Y., Niu, J., Feng, Y., et al. 2022, ATel, 15733